Journal of Anatomy

J. Anat. (2011) **219**, pp481–489 doi: 10.1111/j.1469-7580.2011.01398.x

Visualization of 3D osteon morphology by synchrotron radiation micro-CT

D. M. L. Cooper,[1] B. Erickson,[1] A. G. Peele,[2] K. Hannah,[2] C. D. L. Thomas[3] and J. G. Clement[3]

[1]*Department of Anatomy and Cell Biology, University of Saskatchewan, Saskatoon, SK, Canada*
[2]*ARC Centre of Excellence for Coherent X-ray Science, Department of Physics, La Trobe University, Melbourne, Victoria, Australia*
[3]*University of Melbourne, Melbourne, Victoria, Australia*

Abstract

Cortical bone histology has been the subject of scientific inquiry since the advent of the earliest microscopes. Histology – literally the study of tissue – is a field nearly synonymous with 2D thin sections. That said, progressive developments in high-resolution X-ray imaging are enabling 3D visualization to reach ever smaller structures. Micro-computed tomography (micro-CT), employing conventional X-ray sources, has become the gold standard for 3D analysis of trabecular bone and is capable of detecting the structure of vascular (osteonal) porosity in cortical bone. To date, however, direct 3D visualization of secondary osteons has eluded micro-CT based upon absorption-derived contrast. Synchrotron radiation micro-CT, through greater image quality, resolution and alternative contrast mechanisms (e.g. phase contrast), holds great potential for non-destructive 3D visualization of secondary osteons. Our objective was to demonstrate this potential and to discuss areas of bone research that can be advanced through the application of this approach. We imaged human mid-femoral cortical bone specimens derived from a 20-year-old male (Melbourne Femur Collection) at the Advanced Photon Source synchrotron (Chicago, IL, USA) using the 2BM beam line. A 60-mm distance between the target and the detector was employed to enhance visualization of internal structures through propagation phase contrast. Scan times were 1 h and images were acquired with 1.4-μm nominal isotropic resolution. Computer-aided manual segmentation and volumetric 3D rendering were employed to visualize secondary osteons and porous structures, respectively. Osteonal borders were evident via two contrast mechanisms. First, relatively new (hypomineralized) osteons were evident due to differences in X-ray attenuation relative to the surrounding bone. Second, osteon boundaries (cement lines) were delineated by phase contrast. Phase contrast also enabled the detection of soft tissue remnants within the vascular pores. The ability to discern osteon boundaries in conjunction with vascular and cellular porosity revealed a number of secondary osteon morphologies and provided a unique 3D perspective of the superimposition of secondary osteons on existing structures. Improvements in resolution and optimization of the propagation phase contrast promise to provide further improvements in structural detail in the future.

Key words: cortical bone; Haversian system; micro-CT; osteon; synchrotron.

Introduction

Cortical bone is comprised of a complex collection of microstructural elements, including those that arise through growth and modeling (primary), and those that arise through internal turnover of existing tissue, known as remodeling (secondary). The secondary structures generated by the remodeling process are known as 'secondary osteons' – a term synonymous with 'Haversian systems'. The ability of cortical bone to turnover its internal structure means that this tissue is not only complex, but also dynamic. Due to the central role of remodeling in bone adaptation, maintenance and disease, interest in the regulation of this process remains an important area of inquiry in bone biology. Recent years, for example, have seen the development of increasingly sophisticated *in silico* models to explain the regulation of basic multicellular units (BMUs; Smit & Burger, 2000; Smit et al. 2002; Burger et al. 2003; Martin, 2007; van Oers et al. 2008a,b; Ryser et al. 2009) – the coordinated cellular groupings responsible for the creation of secondary

Correspondence
David M.L. Cooper, Department of Anatomy and Cell Biology, University of Saskatchewan, 107 Wiggins Road, Saskatoon, SK, Canada S7N 5E5. T: +306 966 7895; F: +306 966 4298; E: dml.cooper@usask.ca; davemlcooper@gmail.com

Accepted for publication *27 April 2011*
Article published online *6 June 2011*

osteons (Frost, 1969). These models generally treat the BMU as a cylindrical structure with an osteoclastic cutting cone immediately followed by an osteoblastic closing cone. Indeed, this is the conventional depiction of the BMU that many, including ourselves (Cooper et al. 2003), have reproduced. While this geometry is certainly an appropriate idealization of some osteons, alternative morphologies have been described including drifting/waltzing (Robling & Stout, 1999), branched (Stout et al. 1999) and clustered osteons (Bell et al. 2001; see Cooper et al. 2006; Skedros et al. 2007 for more thorough reviews). Indeed, Johnson's (1964) description of osteon morphology, which just preceded Frost's (1969) formal description of the BMU, included a variety of forms ranging from classic cylindrical to branched and highly irregular forms. The relatively limited 3D data available hint at greater complexity (Amprino, 1948; Cohen & Harris, 1958; Tappen, 1977; Kragstrup & Melsen, 1983; Stout et al. 1999; Moshin et al. 2002) than is generally accounted for in predominant conceptualizations of osteon morphology. Arguably the lack of a wider recognition of the variation in osteon structure is, in part, due to lack of efficient 3D methodologies, and hence studies yielding relevant volumetric information. Ultimately, a more complete understanding of cortical remodeling requires a 3D (spatial) and even 4D (spatial-temporal) appreciation of this tissue's microarchitecture. Such data will not only provide an opportunity to better test existing models of spatial regulation of remodeling, but will undoubtedly lead to novel insights that will improve our understanding of bone adaptation, aging and disease. To date, the most effective means of assessing osteon structure in 3D is serial sectioning – a destructive and tedious method. Micro-computed tomography (micro-CT), a non-destructive X-ray-based approach, has facilitated an advance into the third dimension for the analysis of both trabecular and cortical bone. That said, conventional micro-CT has been limited to the cortical canal network (Cooper et al. 2003, 2006, 2007a,b; Jones et al. 2004; Basillais et al. 2007; Renders et al. 2007; Chen et al. 2010; Pazzaglia et al. in press), and has not enabled direct assessment of secondary osteons (Cooper et al. 2004). Synchrotron radiation (SR) micro-CT benefits from increased brilliance that is orders of magnitude greater than conventional X-ray sources. This improves image quality, reduces scan time, enables higher resolution and facilitates the use of monochromatic (single energy) X-rays (Peyrin, 2009). The improved resolution has, for example, enabled the visualization of cortical vascular canals in smaller animals such as the rat (Matsumoto et al. 2006, 2007), and even osteocyte lacunae in the mouse (Schneider et al. 2007, 2009). The improved image quality of SR micro-CT has also resulted in some success in 2D visualization/segmentation of osteons based upon absorption contrast (Dalstra et al. 2004, 2006; Peter et al. 2007). To our knowledge, however, 3D renderings of osteons from such data have not been published. This may, in part, reflect the fact that density differences between osteons and the surrounding bone can be subtle and inconsistent – complicating direct 3D rendering from attenuation values. An unexplored capability of SR micro-CT in this context is the potential for generating image contrast from differences in the X-ray refractive index within a target. This contrast, known as 'phase contrast' (Wilkins et al. 1996; Mayo et al. 2003; Stevenson et al. 2003; Meuli et al. 2004; Rustichelli et al. 2004; Betz et al. 2007; Zhou & Brahme, 2008; Gureyev et al. 2009), enhances object boundaries and can reveal structures not visible using absorption contrast alone. Phase contrast, for example, is particularly powerful for imaging soft tissues such as cartilage (Zehbe et al. 2010), and can also reveal fine structural variations within mineralized tissues such as striae of Retzius in teeth (Tafforeau & Smith, 2008). Such dental striae are of comparable scale to features in cortical bone such as cement lines (osteon boundaries) and individual bony lamellae. This suggests that visualization of osteons should be enhanced with phase contrast, and thus 3D segmentation should be possible from SR micro-CT datasets. Our objective, therefore, was to non-destructively image secondary osteons in human cortical bone and visualize them in 3D.

Materials and methods

Bone samples

Sub-samples of a single human femur were derived from the Melbourne Femur Collection held in the Melbourne Dental School, University of Melbourne. These samples were prepared from the proximal femur of a 20-year-old male who had died suddenly with no known disease or treatment regimen that could have affected his bones. The collection and study of bone for the work described in this paper was supervised by the Human Research Ethics Committee of the Victorian Institute of Forensic Medicine (EC26/2000) and the Health Sciences Human Ethics Sub-Committee of the University of Melbourne (HREC 980139). An institutional human ethics certificate (Bio#08-46) was also issued at the University of Saskatchewan to approve this work.

The bone was cleaned of soft tissue and preserved in 70% v/v ethanol/water. Two 35-mm-long blocks were cut from the proximal diaphysis using a hacksaw. From these diaphyseal rings, 2-mm-thick slabs were sawn from the anterior, posterior, medial and lateral quadrants using a sawing microtome (Leitz 1600, Wetzlar, Germany) with an annular diamond blade. These were further divided into 2-mm-square 'matchsticks' 35 mm long. See Fig. 1 for detailed information pertaining to the location of the samples within the diaphyseal cross-section. Image data from three of these samples are included in the current study.

Micro-CT configuration and imaging

Synchrotron radiation micro-CT imaging was carried out at the Advanced Photon Source, Argonne National Laboratory on beam line 2BM (# 2 Bending Magnet). Monochromatic X-rays with photon energy of 26.4 keV were collimated into a beam 3 mm wide $\times$ 2 mm high. The energy chosen gives approximately 40%

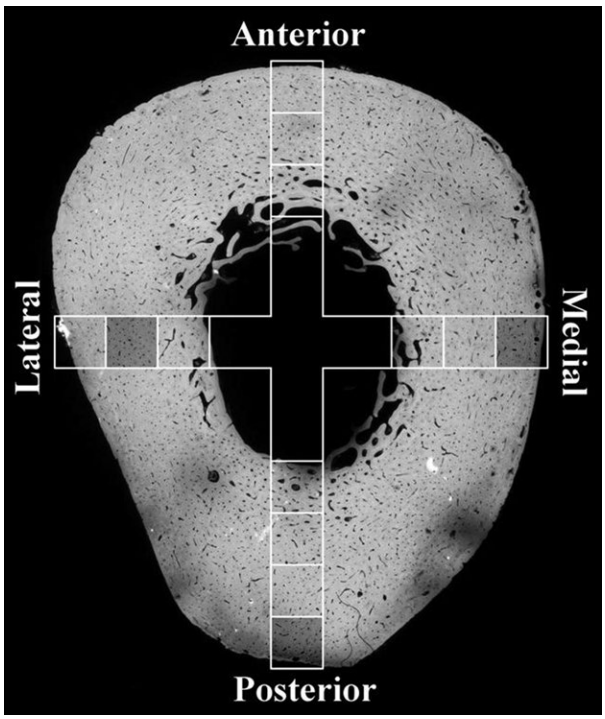

Fig. 1 Schematic overlay of ~ 2 mm × 2 mm samples (squares) over a microradiograph generated from an adjacent block. Shaded squares indicate the sources of the samples explored further below.

transmission through 2 mm of bone (assumed to be pure hydroxyapatite). Transmitted X-rays were converted to visible light with a cadmium tungstate scintillator and the images captured using a CCD camera with 2048 × 2048 pixels, the active region of interest being limited to 1400 pixels high × 2048 pixels wide by the rectangular beam cross-section. An objective lens was chosen to give a theoretical isotropic voxel size of 1.4 μm when the scintillator to object distance was 60 mm. The 60-mm distance enabled the propagation of phase shifts (Zhou & Brahme, 2008). Specimens were either mounted using a specially designed kinematic mount compatible with the robot sample handling system at 2BM or, where use of those mounts restricted sample size, using modeling clay to attach samples to a plain kinematic base. Mounted samples were positioned using high-precision three-axis stages and rotated in the beam at 0.125 ° steps to give 1440 projection images, each stored image being the average of four frames. Each scan took 1 h and produced about 100 Gb of data. For several samples, multiple adjacent scans were acquired to produce a larger volumetric field of view (e.g. osteon in Fig. 4 is 5.3 mm long).

Image reconstruction and analysis

Visualization of osteon boundaries was enhanced by a running z-projection of adjacent slices using ImageJ (NIH; http://rsbweb.nih.gov/ij/) software. Average intensity projections through 10 images (14 μm) were used to aid 3D osteon segmentation. Additional projections (median and minimum intensity) through 100 μm (71 slices at 1.4 μm thickness) were employed to enhance visualization of different features. Osteonal borders were segmented manually using an interactive LCD tablet (Cintiq 12WX model; Wacom, Japan). These outlines were created on intermittent slices and were interpolated for the intervening slices using CTAnalyzer (SkyScan, Aartselaar, Belgium). These interpolated outlines were then visually inspected for accuracy and adjusted if necessary. 3D renders were then generated with the amira 5.2 software package (Visage Imaging, Berlin, Germany). The porous structures were isolated using threshold-driven (automatic) segmentation and the osteonal surfaces were mapped over these structures. This approach enabled the simultaneous visualization of the raw volumetric data and the extracted surfaces in varying degrees of transparency.

Results

The cross-sectional image data revealed vascular canals as well as cellular-level porosity (osteocyte lacunae; Fig. 2A). Phase contrast was evident in the images as bright halos around the porosity (vascular and lacunar). Projections along the *z* dimension (Fig. 2B–D) enhanced visualization of microstructural features. The boundaries of osteons were discernable – both through differential attenuation and through phase contrast. While some evidence of primary circumferential lamellae was observed (especially Fig. 2C), no evidence of lamellae within osteons was detected. One of the most striking features observed was the presence of soft tissue remnants within the vascular pores. In some cases, what appeared to be vessels were evident (Fig. 3).

The visualization of osteonal borders enabled manual segmentation, and a variety of morphologies were observed including a 'classic' cylindrical osteon with a cutting cone apparent on one end (Fig. 4), an actively drifting osteon (Fig. 5) and a branched osteon which was still forming (Fig. 6). A particularly interesting observation was that of the apparent occlusion of an adjacent canal by the progressing BMU evident in Fig. 4E (evident in 3D in Fig. 4B and C).

Discussion

We achieved non-destructive 3D visualization of secondary osteons within human cortical bone. This confirms that synchrotron technology holds great potential to shed new light on cortical bone microarchitectural dynamics. That said, not all osteon borders were consistently visualized and automatic segmentation was not possible. Further, finer scale features (e.g. lamellae within osteons) were not observed. Tafforeau & Smith (2008) observed striae of Retzius in a fossil tooth using 0.7-μm pixel size (half that of the current study). Undoubtedly, application of higher resolution would reveal additional features within cortical bone; however, improved resolution often comes with a trade-off in terms of decreased field of view. An alternative avenue to explore for improved delineation of osteons is the optimization of the specimen-to-detector distance for phase contrast. Zehbe et al. (2010), for example, found that a

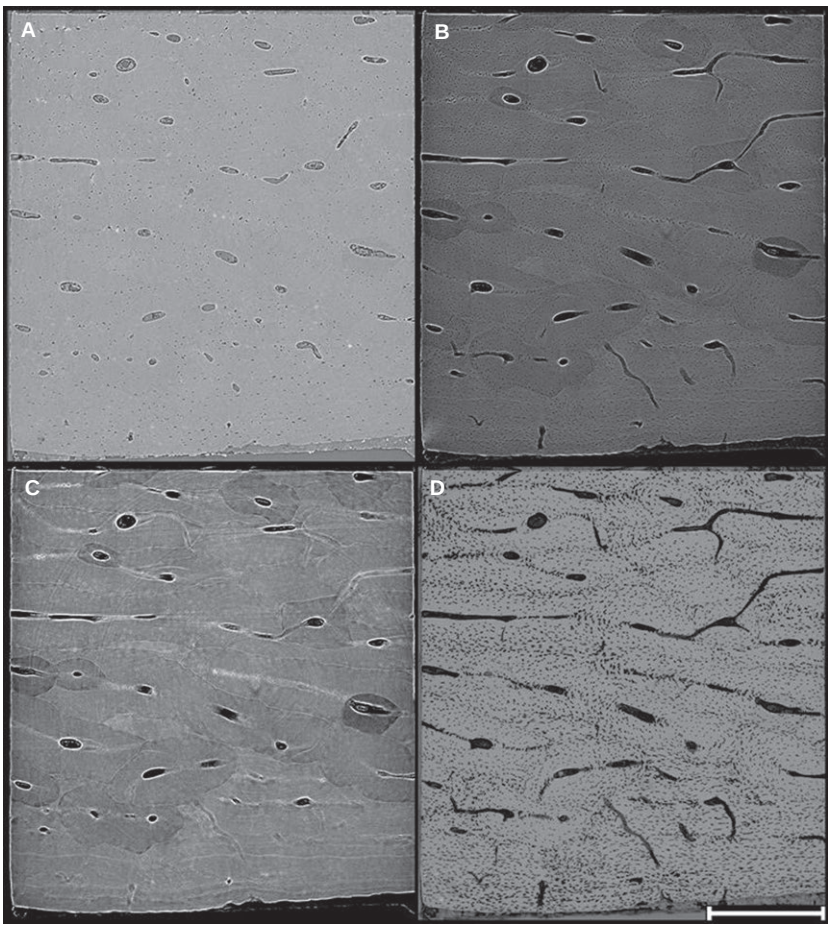

Fig. 2 Representative images from the posterior block located at the periosteal surface of the linea aspera (see Fig. 1). (A) Single SR micro-CT cross-sectional image (1.4 μm isotropic voxels). (B) Average projection through 100 μm. (C) Median projection through 100 μm. (D) Minimum projection through 100 μm, highlighting pores. Scale bar at bottom right is 500 μm long.

100-cm distance to detector best highlighted structural details in their bone/cartilage samples, whereas a shorter distance (15 cm) provided a compromise between edge enhancement (phase contrast) and attenuation contrast. With our relatively small detector to target distance, our images consisted primarily of attenuation contrast with enhancement by phase contrast. While hypermineralized rings around vascular canals can be observed in microradiographs, the bright rings we observed were often paired with adjacent dark rings – a feature characteristic of phase contrast. Further, the visualization of soft tissues within many pores – with apparent attenuation equal or greater than bone matrix – is strong evidence for phase contrast. Beyond attenuation and phase contrast, microstructural segmentation may also be enhanced through the addition of morphological data from the osteocyte lacunae. Osteocytes are arranged between the concentric lamellae surrounding osteon canals, and their patterning provides another line of evidence regarding the delineation of osteon borders (Fig. 2D). In the case of the branching osteon (Fig. 6), the minimum projection (E) reveals how the osteocytes are arranged relative to the two canals – suggesting an organizational separation not apparent in the other images. Ultimately, the optimization of scan parameters and the employment of different approaches to segmentation, alone and combined, promise improved visualization of cortical microarchitecture in the future.

The availability of novel 3D data is of significance to a number of areas of active research in bone biology. The simultaneous observation of mineralized and soft tissues, for example, holds tremendous potential to assess the interfaces of bone and its surrounding tissues. Notably, this capability is already being explored to assess cartilage with SR micro-CT (Zehbe et al. 2010). More relevant to the focus of the current discussion is the possibility of examining internal bone–soft tissue interfaces within the cortical vascular porosity. It may, for example, be possible to visualize bone formation within an individual BMU through the detection of unmineralized osteoid. No special care was taken in the current study regarding the preservation of soft tissues within the specimens. Indeed, the specimens had been desiccated in ethanol for a period of several years and were then air-dried prior to imaging. As such, the observation of soft tissue within canals was somewhat unexpected. While soft tissue remnants were observed within resorption spaces (Figs 4D, 5D and 6D), it is not entirely clear if this is osteoid or not. More careful fixation or cryopreservation would better facilitate the visualization

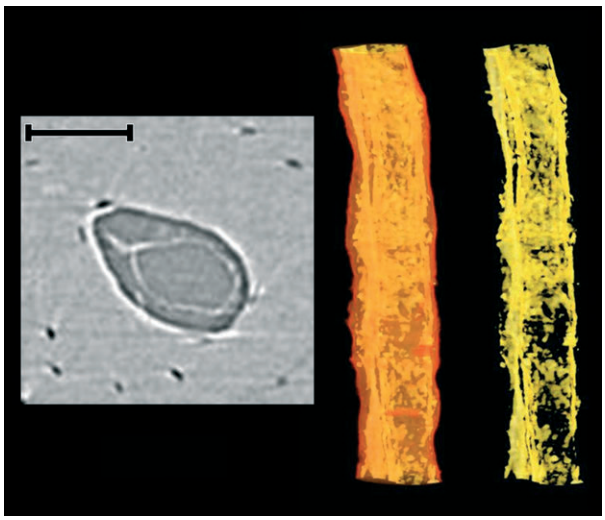

Fig. 3 Soft tissue, possibly a vessel, within vascular pore from the medial periosteal surface (Fig. 1). 2D cross-section image (left); volumetric rendering showing the canal outline in transparency and soft tissue remnants within (middle); isolated soft tissue remnants (right). Scale bar at top left is 100 μm long.

of intact soft tissue elements and their interfaces with the mineralized bone matrix. Specific questions that could be addressed with such an approach include 'how close in proximity are the cutting and closing cones?' and 'how rapid and consistent is the infilling of a resorption space?'.

As already noted, the conventional depiction of the BMU places the closing cone directly adjacent to the cutting cone and the resorption space is rapidly closed. Computer models have relied upon this close spatial relation to link mechanical phenomena with the reversal between bone resorption and formation (Smit & Burger, 2000; Smit et al. 2002; Burger et al. 2003). Conventional micro-CT examination of BMU-related resorption spaces has, however, not provided support for such a close relationship. Indeed, some resorption spaces appear to have no evidence of a closing cone within several millimeters of the cutting cone (Cooper et al. 2006). This may be due to a methodological limitation (e.g. osteoid not being visualized) or may reflect a real lag or quiescent zone between the resorptive and formative phases of the BMU (Johnson, 1964; Parfitt, 1983). Martin (1991) has noted that increasing activation frequency can lead to increased porosity despite maintenance of a balance between the resorption and formation of bone within the individual BMUs. This phenomenon is possible because bone resorption tends to proceed quicker than subsequent formation. Indeed, in one of Johnson's (1964) early depictions of a BMU (fig. 19) – which matches the classic pattern – he noted the slope of the closing cone reflects the infilling rate and this seems to be a disclaimer that his figure was temporally compressed. Johnson estimated a 90-day period was required to fill a 250-μm space when leaving a 50-μm canal. A radial closure of 100 μm over 90 days yields a fill-in rate of approximately 1.1 μm day^{-1}, a value that is in

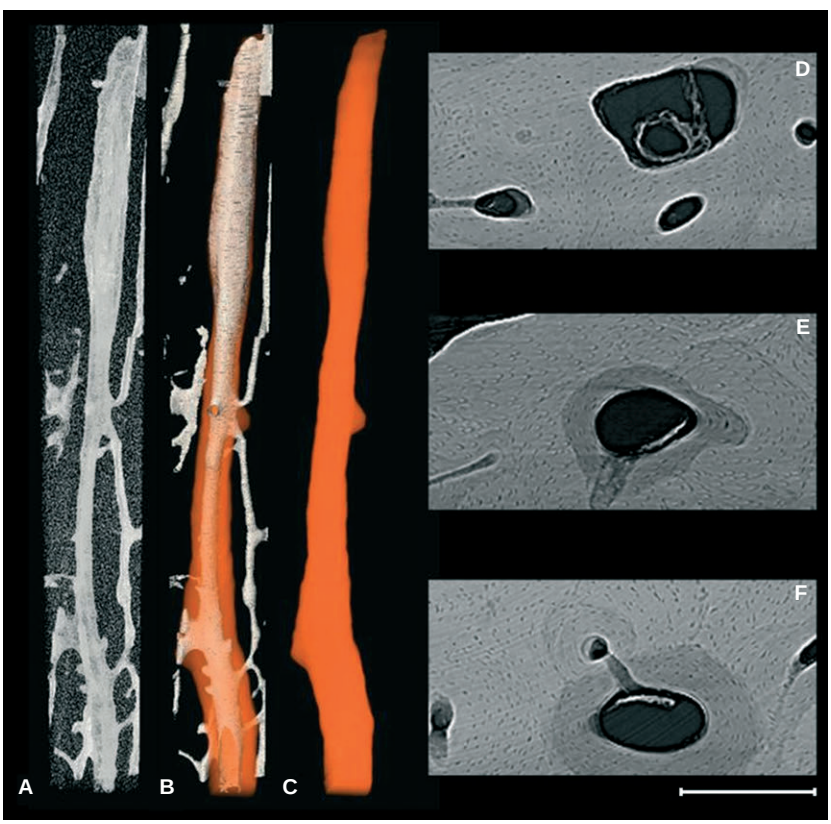

Fig. 4 Representative 3D (A–C) and 2D (D–F) images of a 'classic' forming osteon (active BMU) with roughly cylindrical form from the lateral midcortex (Fig. 1). The porous structures alone (A), vascular porosity with the superimposed osteon outline (B) and finally the osteon outline alone (C) are portrayed in 3D. The 2D images (D–F) are 100 μm average projections roughly corresponding to the adjacent position in the 3D renders. An osteoclastic cutting cone is evident superiorly and the newly forming osteon is progressively filled in inferiorly. The total length of the 3D render is 5.3 mm (stitched together from multiple scans of a single specimen). Scale bar at bottom right is 250 μm long.

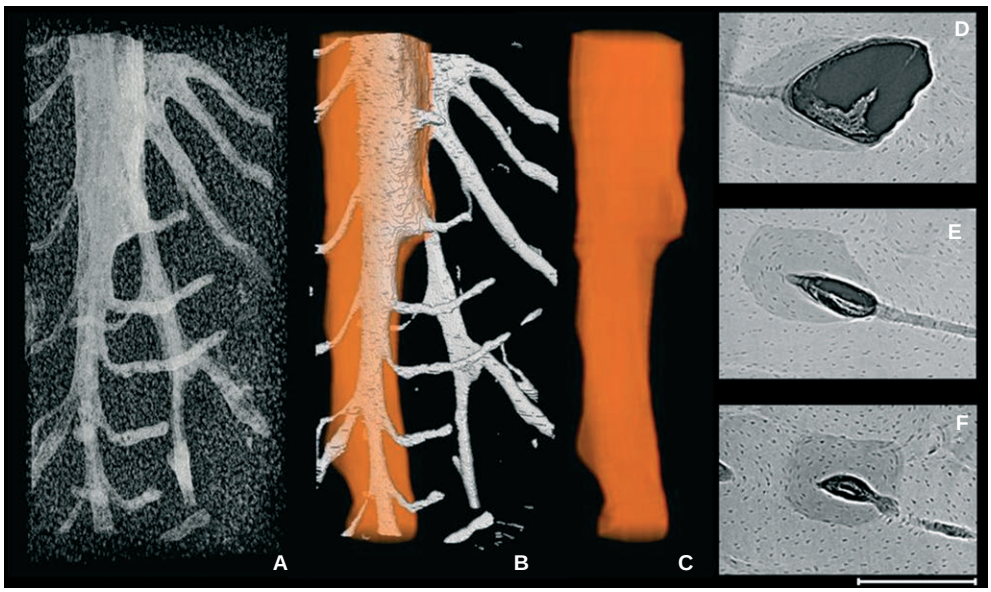

Fig. 5 Representative 3D (A–C) and 2D (D–F) images of a drifting osteon from posterior periosteal surface (Fig. 1). The porous structures alone (A), vascular porosity with the superimposed osteon outline (B) and finally the osteon outline alone (C) are portrayed in 3D. The 2D images (D–F) are 100 μm average projections roughly corresponding to the adjacent position in the 3D render. The sequence clearly shows that the osteon began (F) as roughly cylindrical and then subsequently began to drift (D,E). The cutting cone of the drifting osteon extends beyond the superior aspect of the scan, although a portion of it is evident within (D). The total length of the 3D render is 1.7 mm. Scale bar at bottom right is 250 μm long.

agreement with Frost's (1963) 0.93 μm day^{-1} for healthy human adults. Johnson placed the rate of advance of the cutting cone at 100 μm day^{-1}, a value that is high relative to the 39 μm day^{-1} reported by Jaworski & Lok (1972) in canine bone. These data place the pace of osteoclast resorption at about 40–100 times that of osteoblastic infilling. Thus, we should not expect to see a rapid closure of resorption spaces directly adjacent to the cutting cone as

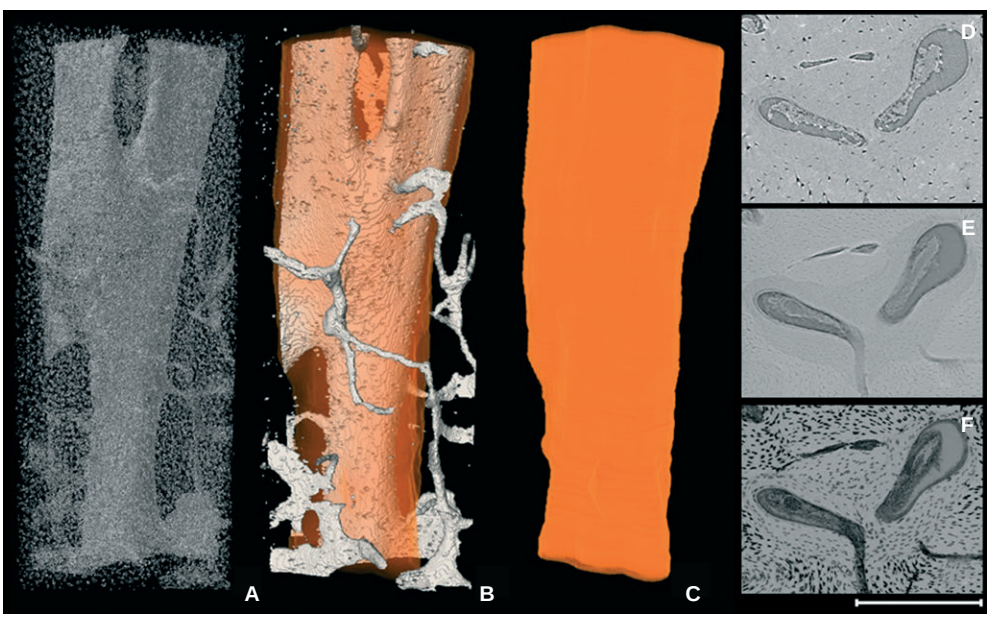

Fig. 6 Representative 3D (A–C) and 2D (D–F) images of a branched osteon medial periosteal surface (Fig. 1). The porous structures alone (A), vascular porosity with the superimposed osteon outline (B) and finally the osteon outline alone (C) are portrayed in 3D. The 2D images are (D) a raw SR micro-CT image; (E) an average projection through 100 μm; and (F) a minimum projection through 100 μm (F). The 2D images (all same location) were produced from the most superior slices used to render the 3D images. The total length of the 3D render is 1.7 mm. Scale bar at bottom right is 250 μm long.

suggested by conventional depictions. Rather, BMUs, such as that depicted in Fig. 4, with long sloping closing cones fit the data better. That said, it is conceivable that the spatial relationship between the cutting and closing cones is variable and may be affected by various stimuli (e.g. hormonal, mechanical), and thus may play an important role in bone balance within a BMU. More and better 3D data are needed to understand this important aspect of the cortical remodeling process.

A related area of inquiry involves the regulation and functional significance of the orientation of secondary osteons. It is generally held that secondary osteons are aligned with the principle stresses experienced by the bone tissue (Hert et al. 1994; Petrtyl et al. 1996). This patterning is proposed to arise through the mechanical regulation of the cutting cone in the active BMU (Smit & Burger, 2000; Smit et al. 2002; Burger et al. 2003). We recently hypothesized that the increasing circularity of osteons observed with aging (Britz et al. 2009) may be due to a change in the orientation of osteons (e.g. increasingly longitudinal with age). Three-dimensional data are ideally suited to answer this question. It has also been proposed that BMUs have the capacity to 'steer' towards defects within cortical bone (Martin, 2007). Similarly, van Oers et al.'s (2008a) model for BMU regulation enables steering of osteons towards areas of apoptotic osteocytes. Abrupt changes in course by active BMUs should leave tell-tale clues, such as sharply curved osteons, which should be discernable with 3D image data. The drifting osteon depicted in Fig. 5 transitions from a cylindrical form (inferior) to a drifting form superiorly. It is unclear what may account for this, but perhaps it is possible that localized stimuli (such as those induced by a microcrack) may have played a role. Again, further investigation is needed to address this proposition.

The degree to which remodeling is directed by microdamage is unclear, with some defining two types of BMUs – targeted and untargeted (Parfitt, 2002). Martin (2002) has posed the question 'is all cortical bone remodeling initiated by microdamage?' – speculating that all remodeling is targeted. Calculating the probability that remodeling is initiated by microcracks is not a simple undertaking as it is based upon a number of assumptions regarding spatial relations (Burr & Martin, 1993). Conventional 2D data are not well suited to definitely address this question. For example, secondary osteons may be many millimeters in length, and the very hypothesis to be tested proposes that evidence of micro-damage will be destroyed by their creation. SR micro-CT may provide the best opportunity to test hypotheses linking the initiation of remodeling to microcracks through 3D visualization of not only BMUs/secondary osteons, but perhaps even the micro-damage (Lee et al. 2003; Thurner et al. 2006; Larrue et al. 2007; Voide et al. 2009) simultaneously.

Most models for the spatial regulation of remodeling employ a simplified geometry and deal with the case of a single osteon. It is unclear if and how such models can explain more complex osteon morphologies including highly branched and clustered forms. Further, BMUs, by their secondary nature, do not pass through a uniform tissue space. Indeed, with progressive age they must navigate through, and interface with, an increasingly complex existing 3D microarchitecture (Cooper et al. 2007b). Our observation of a BMU occluding a neighboring canal (Fig. 4E) reveals the complex 3D behavior of cellular populations. This complex spatio-temporal behavior is sure to challenge existing models for the regulation of remodeling. Finally, the ability to resolve osteocyte lacunae within the context of the secondary osteons will enable a more refined analysis of their density and morphology. A number of recent studies have linked osteocyte morphology with mechanosensing (Vatsa et al. 2008) and disease states (van Hove et al. 2009). Qualitative inspection of our renderings reveals considerable variation in osteocyte density/orientation both within and between osteons. Indeed, a parallel analysis of these scan data has revealed variation in the size of osteocyte lacunae within osteons (Hannah et al. 2010). The mechanisms underpinning variation in osteocyte size, density and orientation are currently unclear, but failing to analyze osteocytes within the larger context of their surrounding microstructural environment risks missing important factors linked to adaptation, aging and disease. A dramatic example of this is that osteons within an individual can vary considerably in age and, in a newly arising disease state, only newly formed osteons would be expected to manifest any differences in osteocyte density (and possibly morphology/orientation).

In the current study we examined a limited number of samples from a single human femur to demonstrate the proof of principle that osteons can be visualized in 3D using phase contrast SR micro-CT. While SR micro-CT affords numerous advantages, it comes with the key limitation of access. There are a limited number of such facilities in the world, and beam time will always be a limiting factor. The best use of this technology is thus likely to be as a supplement to conventional micro-CT and histology – targeted to key questions that are not readily addressed in alternative ways. A key potential, yet to be explored, is the possibility of *in vivo* animal imaging of cortical microarchitecture – which would benefit from the potential of reduced dose from high-energy imaging relying upon phase rather than attenuation contrast.

Concluding remarks

While the study of cortical microstructure extends back to the advent of the earliest microscopes (Cooper et al. 2003), it has largely remained in the 2D realm and thus our understanding of the 3D complexity of this tissue has remained limited. Conventional micro-CT has enabled the shift to 3D analysis of cortical porosity, and SR micro-CT is contributing

further microstructural details including osteocyte lacunae and secondary osteon structure. This powerful tool can be brought to bear to address a number of important questions in bone biology, and will shed new light on our understanding of the complex and dynamic nature of cortical bone.

Acknowledgements

The authors thank Professor Stephen Cordner, Director of the Victorian Institute of Forensic Medicine, and the staff of the mortuary and the Donor Tissue Bank for their assistance in the collection of the bone specimen used in this study. They are also particularly grateful to the next-of-kin of the donors for permission to remove bone for research purposes. The authors additionally acknowledge the Australian Synchrotron Research Program, which is funded by the Commonwealth of Australia under the Major National Research Facilities Program. Use of the Advanced Photon Source was supported by the US DOE, Basic Energy Sciences, Office of Science under Contract No. W-31-109-Eng-38. Data were collected at the APS with the help of the beamline scientist for 2BM, Dr Francesco DeCarlo, whose assistance is gratefully acknowledged. DMLC receives support for this work from the Natural Science and Engineering Research Council of Canada in the form of a Discovery Grant (353618-2008).

Author contributions

D.M.L. Cooper, data analysis/interpretation, drafting of the manuscript. B. Erickson, data analysis/interpretation. A. G. Peele, acquisition of data, critical revision of the manuscript. K. Hannah, acquisition of data. C.D.L. Thomas, acquisition of data, critical revision of the manuscript, approval of the article. J.G. Clement, contributions to concept/design, critical revision of the manuscript, approval of the article.

References

Amprino R (1948) A contribution to the functional meaning of the substitution of primary by secondary bone tissue. *Acta Anat*, **5**, 291–300.

Basillais A, Bensamoun S, Chappard C, et al. (2007) Three-dimensional characterization of cortical bone microstructure by microcomputed tomography: validation with ultrasonic and microscopic measurements. *J Orthop Sci*, **12**, 141–148.

Bell KL, Loveridge N, Reeve J, et al. (2001) Super-osteons (remodeling clusters) in the cortex of the femoral shaft: influence of age and gender. *Anat Rec*, **264**, 378–386.

Betz O, Wegst U, Weide D, et al. (2007) Imaging applications of synchrotron X-ray phase-contrast microtomography in biological morphology and biomaterials science. I. General aspects of the technique and its advantages in the analysis of millimetre-sized arthropod structure. *J Microsc*, **227**, 51–71.

Britz HM, Thomas CD, Clement JG, et al. (2009) The relation of femoral osteon geometry to age, sex, height and weight. *Bone*, **45**, 77–83.

Burger EH, Klein-Nulend J, Smit TH (2003) Strain-derived canalicular fluid flow regulates osteoclast activity in a remodelling osteon – a proposal. *J Biomech*, **36**, 1453–1459.

Burr DB, Martin RB (1993) Calculating the probability that microcracks initiate resorption spaces. *J Biomech*, **26**, 613–616.

Chen H, Zhou X, Shoumura S, et al. (2010) Age- and gender-dependent changes in three-dimensional microstructure of cortical and trabecular bone at the human femoral neck. *Osteoporos Int* **21**, 627–636.

Cohen J, Harris W (1958) The three-dimensional anatomy of haversian systems. *J Bone Joint Surg Am*, **40A**, 419–434.

Cooper DM, Turinsky AL, Sensen CW, et al. (2003) Quantitative 3D analysis of the canal network in cortical bone by micro-computed tomography. *Anat Rec B New Anat*, **274**, 169–179.

Cooper DM, Matyas JR, Katzenberg MA, et al. (2004) Comparison of microcomputed tomographic and microradiographic measurements of cortical bone porosity. *Calcif Tissue Int*, **74**, 437–447.

Cooper DM, Thomas CD, Clement JG, et al. (2006) Three-dimensional microcomputed tomography imaging of basic multicellular unit-related resorption spaces in human cortical bone. *Anat Rec A Discov Mol Cell Evol Biol*, **288**, 806–816.

Cooper D, Turinsky A, Sensen C, et al. (2007a) Effect of voxel size on 3D micro-CT analysis of cortical bone porosity. *Calcif Tissue Int*, **80**, 211–219.

Cooper DM, Thomas CD, Clement JG, et al. (2007b) Age-dependent change in the 3D structure of cortical porosity at the human femoral midshaft. *Bone*, **40**, 957–965.

Dalstra M, Karaj E, Beckmann F, et al. (2004) Osteonal mineralization patterns in cortical bone studied by synchrotron radiation-based computed microtomography and scanning accoustic microscopy. In *Developments in X-ray Tomography IV Proc. of SPIE Vol. 5535* (ed. Bonse U), pp. 144–151. Bellingham: SPIE.

Dalstra M, Cattaneo PM, Beckmann F (2006) Synchrotron radiation-based microtomography of alveolar support tissues. *Orthod Craniofac Res*, **9**, 199–205.

Frost HM (1963) Mean formation time of human osteons. *Can J Biochem Physiol*, **41**, 1307–1310.

Frost HM (1969) Tetracycline-based histological analysis of bone remodeling. *Calcif Tissue Res*, **3**, 211–237.

Gureyev TE, Mayo SC, Myers DE, et al. (2009) Refracting Rontgen's rays: propagation-based x-ray phase contrast for biomedical imaging. *J Appl Phys*, **105**, 12.

Hannah KM, Thomas CD, Clement JG, et al. (2010) Bimodal distribution of osteocyte lacunar size in the human femoral cortex as revealed by micro-CT. *Bone*, **47**, 866–871.

Hert J, Fiala P, Petrtyl M (1994) Osteon orientation of the diaphysis of the long bones in man. *Bone*, **15**, 269–277.

van Hove RP, Nolte PA, Vatsa A, et al. (2009) Osteocyte morphology in human tibiae of different bone pathologies with different bone mineral density – is there a role for mechanosensing? *Bone*, **45**, 321–329.

Jaworski ZF, Lok E (1972) The rate of osteoclastic bone erosion in Haversian remodeling sites of adult dog's rib. *Calcif Tissue Res*, **10**, 103–112.

Johnson LC (1964) Morphologic analysis of pathology. In *Bone Biodynamics* (ed. Frost HM), pp. 543–654. Boston: Little, Brown, and Company.

Jones AC, Milthorpe B, Averdunk H, et al. (2004) Analysis of 3D bone ingrowth into polymer scaffolds via micro-computed tomography imaging. *Biomaterials*, **25**, 4947–4954.

Kragstrup J, Melsen F (1983) Three-dimensional morphology of trabecular bone osteons reconstructed from serial sections. *Metab Bone Dis Relat Res*, **5**, 127–130.

Larrue A, Rattner A, Laroche N, et al. (2007) Feasibility of microcrack detection in human trabecular bone images from 3D synchrotron microtomography. *Conf Proc IEEE Eng Med Biol Soc*, **2007**, 3918–3921.

Lee TC, Mohsin S, Taylor D, et al. (2003) Detecting microdamage in bone. *J Anat*, **203**, 161–172.

Martin RB (1991) On the significance of remodeling space and activation rate changes in bone remodeling. *Bone*, **12**, 391–400.

Martin RB (2002) Is all cortical bone remodeling initiated by microdamage? *Bone*, **30**, 8–13.

Martin RB (2007) Targeted bone remodeling involves BMU steering as well as activation. *Bone*, **40**, 1574–1580.

Matsumoto T, Yoshino M, Asano T, et al. (2006) Monochromatic synchrotron radiation muCT reveals disuse-mediated canal network rarefaction in cortical bone of growing rat tibiae. *J Appl Physiol*, **100**, 274–280.

Matsumoto T, Yoshino M, Uesugi K, et al. (2007) Biphasic change and disuse-mediated regression of canal network structure in cortical bone of growing rats. *Bone*, **41**, 239–246.

Mayo SC, Davis TJ, Gureyev TE, et al. (2003) X-ray phase-contrast microscopy and microtomography. *Opt Express*, **11**, 2289–2302.

Meuli R, Hwu Y, Je JH, et al. (2004) Synchrotron radiation in radiology: radiology techniques based on synchrotron sources. *Eur Radiol*, **14**, 1550–1560.

Moshin S, Taylor D, Lee TC (2002) Three-dimensional reconstruction of Haversian systems in ovine compact bone. *Eur J Morphol*, **40**, 309–315.

van Oers RF, Ruimerman R, Tanck E, et al. (2008a) A unified theory for osteonal and hemi-osteonal remodeling. *Bone*, **42**, 250–259.

van Oers RF, Ruimerman R, van Rietbergen B, et al. (2008b) Relating osteon diameter to strain. *Bone*, **43**, 476–482.

Parfitt AM (1983) The physiologic and clinical significance of bone histomorphometric data. In *Bone Histomorphometry: Techniques and Interpretation* (ed. Recker RR), pp. 143–222. Boca Raton: CRC Press.

Parfitt AM (2002) Targeted and nontargeted bone remodeling: relationship to basic multicellular unit origination and progression. *Bone*, **30**, 5–7.

Pazzaglia UE, Zarattini G, Giacomini D, et al. (in press) Morphometric analysis of the canal system of cortical bone: an experimental study in the rabbit femur carried out with standard histology and micro-CT. *Anat Histol Embryol*, **39**, 17–26.

Peter Z, Bousson V, Bergot C, et al. (2007) Segmentation of low contrast features in bone micro-CT images by a constrained region growing approach based on watershed. In *4th IEEE Symposium on Biomedical Imaging: from Nano to Macro*, pp. 968–971. Proceedings of the 4th IEEE Symposium on Biomedical Imaging: from Nano to Macro, pp. 968–971. Arlington: IEEEXplore. Available at http://dx.doi.org/10.1109/ISBI.2007.357015.

Petrtyl M, Hert J, Fiala P (1996) Spatial organization of the haversian bone in man. *J Biomech*, **29**, 161–169.

Peyrin F (2009) Investigation of bone with synchrotron radiation imaging: from micro to nano. *Osteoporos Int*, **20**, 1057–1063.

Renders GA, Mulder L, van Ruijven LJ, et al. (2007) Porosity of human mandibular condylar bone. *J Anat*, **210**, 239–248.

Robling AG, Stout SD (1999) Morphology of the drifting osteon. *Cells Tissues Organs*, **164**, 192–204.

Rustichelli F, Romanzetti S, Dubini B, et al. (2004) Phase-contrast microtomography of thin biomaterials. *J Mater Sci Mater Med*, **15**, 1053–1057.

Ryser MD, Nigam N, Komarova SV (2009) Mathematical modeling of spatio-temporal dynamics of a single bone multicellular unit. *J Bone Miner Res*, **24**, 860–870.

Schneider P, Stauber M, Voide R, et al. (2007) Ultrastructural properties in cortical bone vary greatly in two inbred strains of mice as assessed by synchrotron light based micro- and nano-CT. *J Bone Miner Res*, **22**, 1557–1570.

Schneider P, Krucker T, Meyer E, et al. (2009) Simultaneous 3D visualization and quantification of murine bone and bone vasculature using micro-computed tomography and vascular replica. *Microsc Res Tech*, **72**, 690–701.

Skedros JG, Sorenson SM, Jenson NH (2007) Are distributions of secondary osteon variants useful for interpreting load history in mammalian bones? *Cells Tissues Organs*, **185**, 285–307.

Smit TH, Burger EH (2000) Is BMU-coupling a strain-regulated phenomenon? A finite element analysis. *J Bone Miner Res*, **15**, 301–307.

Smit TH, Burger EH, Huyghe JM (2002) A case for strain-induced fluid flow as a regulator of BMU-coupling and osteonal alignment. *J Bone Miner Res*, **17**, 2021–2029.

Stevenson AW, Gureyev TE, Paganin D, et al. (2003) Phase-contrast X-ray imaging with synchrotron radiation for materials science applications. *Nucl Instrum Methods Phys Res B*, **199**, 427–435.

Stout SD, Brunsden BS, Hildebolt CF, et al. (1999) Computer-assisted 3D reconstruction of serial sections of cortical bone to determine the 3D structure of osteons. *Calcif Tissue Int*, **65**, 280–284.

Tafforeau P, Smith TM (2008) Nondestructive imaging of hominoid dental microstructure using phase contrast X-ray synchrotron microtomography. *J Hum Evol*, **54**, 272–278.

Tappen NC (1977) Three-dimensional studies of resorption spaces and developing osteons. *Am J Anat*, **149**, 301–332.

Thurner PJ, Wyss P, Voide R, et al. (2006) Time-lapsed investigation of three-dimensional failure and damage accumulation in trabecular bone using synchrotron light. *Bone*, **39**, 289–299.

Vatsa A, Breuls RG, Semeins CM, et al. (2008) Osteocyte morphology in fibula and calvaria – is there a role for mechanosensing? *Bone*, **43**, 452–458.

Voide R, Schneider P, Stauber M, et al. (2009) Time-lapsed assessment of microcrack initiation and propagation in murine cortical bone at submicrometer resolution. *Bone*, **45**, 164–173.

Wilkins SW, Gureyev TE, Gao D, et al. (1996) Phase-contrast imaging using polychromatic hard X-rays. *Nature*, **384**, 335–338.

Zehbe R, Haibel A, Riesemeier H, et al. (2010) Going beyond histology. Synchrotron micro-computed tomography as a methodology for biological tissue characterization: from tissue morphology to individual cells. *J R Soc Interface*, **7**, 49–59.

Zhou SA, Brahme A (2008) Development of phase-contrast X-ray imaging techniques and potential medical applications. *Phys Med*, **24**, 129–148.